The Astrophysical Journal Letters, 904:L22 (9pp), 2020 December 1 https://doi.org/10.3847/2041-8213/abc894

Investigating the Hubble Constant Tension: Two Numbers in the Standard Cosmological Model

Weikang Lin[1], Katherine J. Mack[1,2], and Liqiang Hou[1]
[1] Physics Department, North Carolina State University, Raleigh, NC 27695, USA; wlin23@ncsu.edu
[2] Perimeter Institute for Theoretical Physics, Waterloo, ON N2L 2Y5, Canada
Received 2019 December 12; revised 2020 November 8; accepted 2020 November 9; published 2020 November 27

Abstract

The current Hubble constant tension is usually presented by comparing constraints on H_0 only. However, the postrecombination background cosmic evolution is determined by two parameters in the standard ΛCDM model, the Hubble constant (H_0) and today's matter energy fraction (Ω_m). If we therefore compare all constraints individually in the H_0–Ω_m plane, (1) various constraints can be treated as independently as possible, (2) single-sided constraints are easier to consider, (3) compatibility among different constraints can be viewed in a more robust way, (4) the model dependence of each constraint is clear, and (5) whether or not a nonstandard model is able to reconcile all constraints in tension can be seen more effectively. We perform a systematic comparison of different constraints in the H_0–Ω_m space based on a flat ΛCDM model, treating them as separately as possible. Constraints along different degeneracy directions consistently overlap in one region of the space, with the local measurement from Cepheid variable–calibrated supernovae being the most outlying, followed by the time-delay strong-lensing result. Considering the possibility that some nonstandard physics may reconcile the constraints, we provide a general discussion of nonstandard models with modifications at high, mid, or low redshifts and the effect of local environmental factors. Due to the different responses of individual constraints to a modified model, it is not easy for nonstandard models to reconcile all constraints if none of them have unaccounted-for systematic effects.

Unified Astronomy Thesaurus concepts: Cosmology (343); Hubble constant (758); Cosmological models (337); Expanding universe (502)

1. Introduction

Cosmology used to be called "a search for two numbers," referring to the Hubble constant and the deceleration parameter (Sandage 1970). While the former describes today's cosmic expansion rate and, when first discovered, caused Einstein to abandon his idea of the cosmological constant Λ, the latter turned out to be negative and prompted physicists to bring Λ back. Dubbed (flat) "ΛCDM," the simplest cosmological model fully determines the dynamics of the homogeneous universe with another combination of two numbers, this time pairing the Hubble constant H_0 with today's matter energy fraction Ω_m. Together with its description of large-scale inhomogeneities, this model has successfully explained various cosmological and astronomical observations. Its simplicity and (at least overall) concordance has made it the standard cosmological model, even while named after its two most mysterious aspects. The two numbers, H_0 and Ω_m, are the focus of this work.

Despite its successes, some tensions have recently been reported between observations based on the standard cosmological model. Among them, the Hubble constant tension is one of the most hotly debated; the local determination of H_0 based on Cepheid variable–calibrated Type Ia supernovae (SNe Ia; Riess et al. 2019) is higher than the one inferred from cosmic microwave background (CMB) observations (Planck Collaboration et al. 2018) at a 4.4σ confidence level, a discrepancy that has kept increasing with more precise data from both sides in the past decade. For the time being, it is unclear whether this tension is caused by some new physics beyond the standard cosmological model or some systematic effects in either or both of the measurements.

Looking for other independent observations is important and pressing, as this can help us to draw a more robust conclusion on the cause of the H_0 tension. Unfortunately, most other constraints on H_0 are not currently precise enough to settle the question, and their model dependences make the comparison more difficult to interpret. Nonetheless, ΛCDM can be taken as the default model to which all others can be compared. And because there are two parameters (H_0 and Ω_m) that specify the background evolution in ΛCDM, we should not compare constraints only on H_0. It is more instructive to perform a comparison in the H_0–Ω_m space. While other authors sometimes perform this comparison, the benefits of doing so have rarely been discussed in the literature.

Usually, in order to obtain stronger constraints on H_0, different observations are combined to break degeneracies. Doing this not only reduces the number of constraints to compare but also causes the joint results to correlate with each other, as certain constraints are frequently used to break degeneracies (e.g., SNe). The model dependence of a joint result gets more complicated as well, because a new model may change some constraints in a joint study but not others. We will take a different approach and treat constraints as separately as possible; each constraint is obtained using a minimal number of observations (see Appendix C for a discussion about baryon acoustic oscillations, BAOs), and we treat them individually in the H_0–Ω_m plane. In the H_0–Ω_m plane, several such constraints are actually not weak compared to the local determination, because their favored parameter spaces are relatively small. Therefore, it is not necessary for constraints to be strong on H_0 alone in order to be included in the comparison. Comparing constraints in such a way makes it clear which observations, when combined, can break degeneracies to give stronger constraints on H_0 and possible to see if those combinations would push us to unacceptable (H_0, Ω_m) regions. Considering observations individually also allows us to more clearly see which constraint in the H_0–Ω_m plane would be altered in a

nonstandard model, providing information on whether a proposed model can reconcile all constraints and better clarifying the model dependence of each constraint, as advocated by Verde et al. (2019). In addition, general single-sided constraints are easier to include in the H_0–Ω_m plane. We will demonstrate the advantages of this approach here and investigate the current H_0 tension with a thorough comparison of different constraints. We then discuss whether any nonstandard models are capable of reconciling all constraints, assuming systematic effects are not biasing any results.

2. Methods and Results

In order to perform a thorough multiconstraint comparison, we have collected a number of independent constraints in the H_0–Ω_m space obtained from different observations, assuming the standard flat ΛCDM model. We list them below.

Time-delay strong lensing (H0LiCOW). The time-delay distance for strong-lensing systems measures H_0 in a way that is insensitive to the underlying cosmological model. The H0LiCOW constraint is obtained by running the jupyter notebook provided at www.h0licow.org (Wong et al. 2020), which includes six lens systems. We also added to the notebook a seventh lens system (included in Shajib et al. 2020, not publicly released) according to the description in Appendix A. In our numerical analysis, we also consider the recent result from Birrer et al. (2020) as an alternative constraint (TDCOSMO), which relaxed the strong assumption on the lens model as used in Wong et al. (2020).

SN Ia Pantheon (SN P). The relative change of the apparent magnitude of these standard candles as a function of redshift tightly constrains Ω_m (Scolnic et al. 2018).

γ-ray attenuation (γ-ray). The optical depth along the light of sight depends on the cosmic evolution (Domínguez et al. 2019; chains obtained from private conversation).

Dark Energy Survey Year 1 (DES). Correlations among galaxies and cosmic shear puts a constraint mainly in the Ω_m direction (3×2 correlation functions; Abbott et al. 2018; chains obtained from https://des.ncsa.illinois.edu). As most other large-scale structure (LSS) results are fairly uninformative in the H_0–Ω_m plane, we only include the DES constraint here.

Other LSS constraints. Most other LSS constraints on the H_0–Ω_m plane are weak and prior-limited. Here we consider two more constraints on this plane: galaxy clusters from the SPT-SZ survey (SPT SZ; Bocquet et al. 2019; chains obtained by using the package from https://pole.uchicago.edu) and relaxed galaxy clusters (Mantz et al. 2014; a constraint on $\Omega_m h^{1/2}$ in their Table 5). We include both constraints in our numerical analysis but only plot SPT SZ in Figure 2 in Appendix D for clarity.

Cosmic chronometers (CCs). The differential ages of passively evolving galaxies at two nearby redshifts directly measure the cosmic expansion rate at that redshift. The constraint here is obtained by performing a likelihood analysis of the data compilation discussed in Moresco & Marulli (2017). We have added the estimated systematic errors considered in Moresco et al. (2020); more details in Appendix B.

Galaxy BAO + BBN (BAO Gal). Galaxy BAOs consist of measurements at $z_{\rm eff} = 0.106$ (Beutler et al. 2011), 0.15 (Ross et al. 2015), 0.38, 0.51, 0.61 (Alam et al. 2017), and 1.52 (Ata et al. 2018).

Lyα BAO + BBN (BAO Lyα). These BAOs are deduced from Lyα autocorrelation at $z = 2.34$ and Lyα–quasar cross-correlation at $z = 2.35$ (Blomqvist et al. 2019). The two BAO constraints are obtained by running the corresponding modules in CosmoMC (Lewis & Bridle 2002) with the big bang nucleosynthesis (BBN) constraint on $\Omega_b h^2 = 0.0222 \pm 0.0005$ (Cooke et al. 2018).

WMAP 2013 (WMAP). The 9 yr Wilkinson Microwave Anisotropy Probe CMB data provides an powerful constraint on the standard ΛCDM model (Hinshaw et al. 2013).

Planck 2018 (Planck). Full-mission Planck baseline CMB temperature and polarization data puts an even stronger constraint on the standard model than WMAP (Planck Collaboration et al. 2018). Chains of both WMAP and Planck are obtained from https://pla.esac.esa.int.

Cepheid-calibrated SNe Ia (CV SNe). This local determination of H_0 uses SNe Ia calibrated by Cepheid variables (Riess et al. 2019). There is a small correlation between the SN P constraint on Ω_m and the local measurement on H_0, which we ignore; also see Dhawan et al. (2020) for discussion.

Alternative local measurements. For the purpose of our numerical analysis, we also consider the result from the megamaser cosmology project (MCP; Pesce et al. 2020) as an independent local measurement, as well as the tip-of-the-red-giant-branch (TRGB) result from Freedman et al. (2019) as an alternative distance ladder measurement, but for clarity, we do not include these in Figure 1 but rather show them individually in Appendix D.

Cosmic age. The cosmic time since $z = 100$ ($t_{\rm age}^{100}$) should be larger than some estimated stellar ages (t_*).[3] For example, based on a Hubble Space Telescope fine guidance sensor (FGS) parallax, the age of HD 140283 is estimated to be $t_* = 14.27 \pm 0.8$ Gyr (VandenBerg et al. 2014), though this stellar age was recently reestimated to be 13.5 ± 0.7 Gyr using the Gaia DR2 parallax (Jimenez et al. 2019). In addition, Schlaufman et al. (2018) estimated J18082002–5104378 A to have an age of 13.535 ± 0.002 Gyr based on the Dartmouth isochrone library, though this only includes a statistical error. To investigate possible systematic effects, Schlaufman et al. (2018) considered two additional isochrone libraries, which gave lower estimates. However, they still preferred the higher estimate, since the Dartmouth library accounts for the α-enhanced composition and has a better fit to the data (Schlaufman et al. 2018). More work is needed to arrive at a robust error estimate. Some Galactic globular clusters also have high estimated ages, e.g., 13.4 ± 1.3 Gyr for NGC 5466 and 13.4 ± 1.5 Gyr for NGC 2298, NGC 6101, and NGC 6341 (O'Malley et al. 2017, Table 6). To show how stellar ages put constraints on the H_0–Ω_m plane, we plot three guiding allowed regions (orange) in Figure 1 using the estimated age of J18082002–5104378 A (if confirmed), as well as $t_{\rm age}^{100} > 13$ and 12.5 Gyr. Although the uncertainties are large for most of the stellar ages quoted here, their mean values are consistently higher than the $t_{\rm age}^{100} \simeq 12.7$ Gyr suggested by a ΛCDM universe with $H_0 \simeq 74$ km s^{-1} Mpc^{-1} and $\Omega_m \simeq 0.3$.

[3] We conservatively assume that no stars could have formed before $z = 100$. A larger limiting redshift does not change the bounds significantly. But a larger confirmed stellar age or a later stellar formation time will tighten the bounds toward a smaller-H_0 or smaller-Ω_m direction.

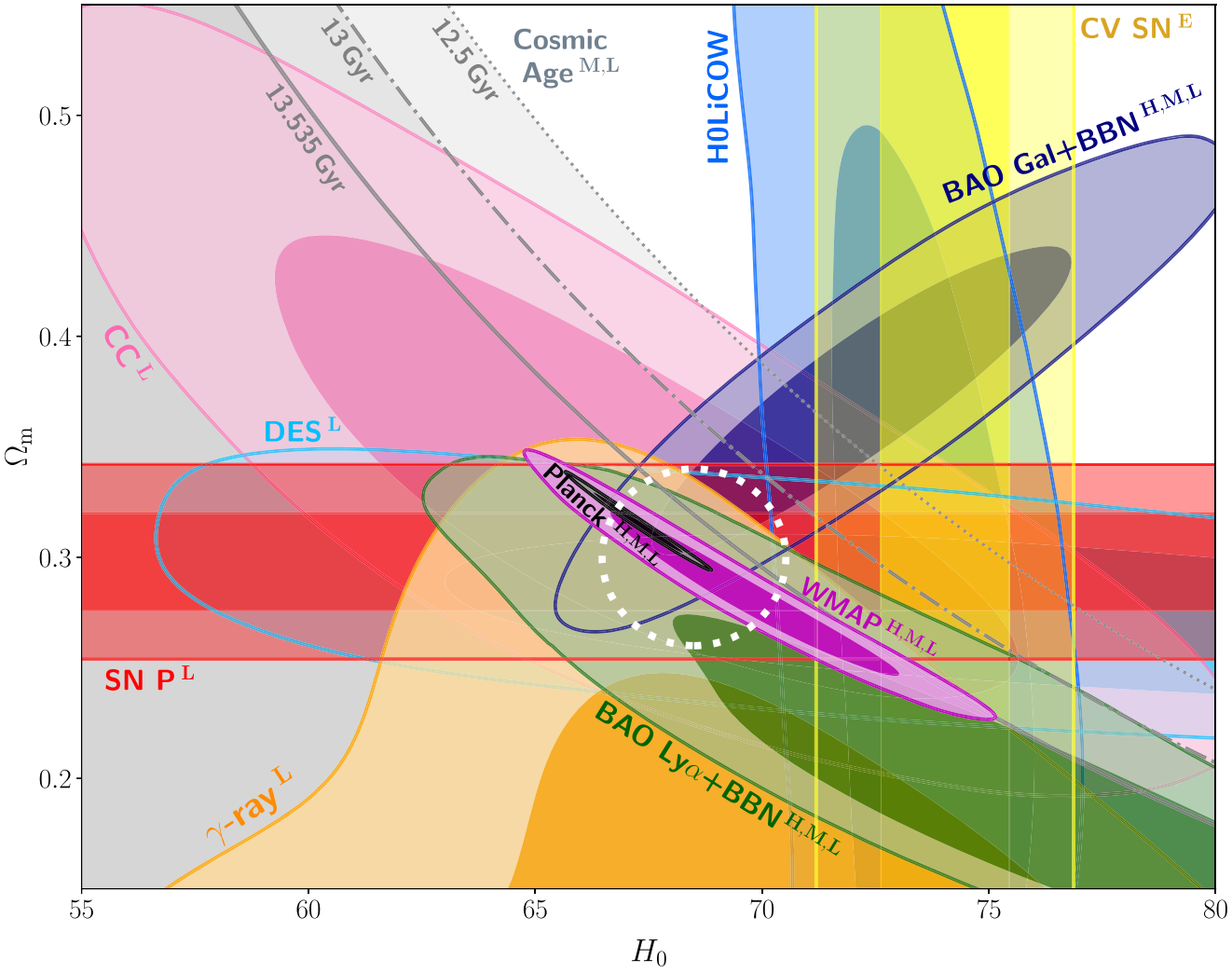

Figure 1. Different constraints in the H_0 and Ω_m space based on a flat ΛCDM model. Dark and light contours show the 68% and 95% confidence regions of each posterior, with the exception of the cosmic-age bounds. (For each of those, the parameter space outside the orange regions is excluded if the universe is at least the age given in the label.) Most constraints with different degeneracy directions consistently overlap the region indicated by the guiding white dashed circle. Note that the circle does not represent a joint constraint. Such a common region is, however, not overlapped by the Cepheid-based local determination of H_0 (CV SN) and is only marginally overlapped by the H0LiCOW constraint. Contours correspond to SN P (red), DES (light blue), CC (pink), H0LiCOW (blue), BAO Gal (navy), BAO Lyα (green), γ-ray (orange), WMAP (magenta), Planck (black), CV SN (yellow), and some guiding cosmic-age constraints ($t_* = 13.535$, 13, and 12.5 Gyr; orange). See the text for descriptions and sources of these constraints. Each constraint in the figure is labeled according to whether it can be changed by nonstandard high-z models (H), mid-z models (M), low-z models (L), or local environmental factors (E). See the text for the definition of these model categories. We leave the H0LiCOW technique without a label because it is relatively insensitive to the underlying cosmological model.

We present all of the above constraints in Figure 1, except the alternative local measurements. We omit these because the uncertainty of the MCP result is relatively large compared to CV SN, and we consider the TRGB-based result (which is consistent with most other constraints) as an alternative to CV SN; we do, however, consider them in our numerical analysis and plot them individually in Appendix D.

To check the consistency of a number of constraints, it is instructive to consider whether there is some common parameter region simultaneously overlapped by them. Note that observations only need to give some favored region in the H_0–Ω_m space; they may not necessarily give strong constraints on H_0. For example, SN P is uninformative on H_0, and the stellar age constraint is only single-sided. Among those constraints, while both the local measurement and the H0LiCOW technique are insensitive to a cosmological model, other constraints are more model-dependent. However, being model-insensitive does not mean being free from systematic effects, which may affect any result. We therefore first analyze such a multiconstraint comparison based on the standard cosmology, taking the face values of those constraints reported in the literature. Possible unaccounted-for errors for particular observations and nonstandard cosmological models will be discussed later.

We can see in Figure 1 that most constraints overlap at a common parameter space indicated by the guiding white dashed circle. We stress that this circle is a guide, not a joint constraint. Importantly, the overlapping constraints are along different degeneracy directions, which more robustly shows that these constraints are consistent with each other. This point cannot be seen from a comparison of constraints on H_0 alone. In the standard ΛCDM model, two constraints, CV SN and H0LiCOW, are noticeably incompatible with the other constraints. Their overlap with other constraints occurs at different parameter regions, depending on which constraints we wish to reconcile. Roughly speaking, they overlap best with

Table 1
Multidata Set IOIs and $\mathcal{O}_j$ for Our Considered Constraints (Not Including the Cosmic-age Bounds)

(IOI) and $\mathcal{O}_j$	CV SN	Planck	H0LiCOW	BAO Gal	Others
All (3.71)	6.74	4.22	4.22	2.41	<1.8
~~SN~~ (2.81)	N/A	1.97	5.12	1.43	<2.0
~~CVSN, H0LiCOW~~ (2.08)	N/A	0.80	N/A	1.62	<2.1
~~WMAP~~ (3.71)	6.75	5.28	4.22	2.41	<1.8
~~Planck~~ (3.07)	3.96	N/A	2.19	4.31	<1.7
TRGB ~~CVSN~~ (2.62)	N/A	2.13	4.99	1.42	<1.9
TDCOSMO ~~H0LiCOW~~ (2.77)	7.66	2.41	N/A	1.55	<1.9
Combined BAO (3.24)	6.87	3.87	2.94	N/A	<1.8

Note. If one constraint has a significantly higher $\mathcal{O}_j$ than the others, it is considered outlying. The first row is the analysis of all constraints; the MCP result is included in the analysis. The second to fifth rows are those after removing CV SN, CV SN and H0LiCOW, WMAP, and Planck, respectively. We replace CV SN with TRGB in the sixth row and replace H0LiCOW with TDCOSMO in the seventh row. In the eighth row, we combine the two BAO results.

BAO Gal at $\Omega_m \sim 0.4$, SN P and DES at $\Omega_m \sim 0.3$, and BAO Lyα, γ-ray attenuation, and WMAP at $\Omega_m \sim 0.23$. If a star is confirmed to be older than 13 Gyr, CV SN and H0LiCOW would overlap with the cosmic-age constraint at $\Omega_m \lesssim 0.27$, and at an even lower range with a higher stellar age.

It is useful to find a numerical way to quantify and generalize the above multiconstraint comparison. To do that, we use the momentum-based multidata set Index of Inconsistency (IOI; Lin & Ishak 2017) and the associated "outlier index" ($\mathcal{O}_j$; Lin & Ishak 2019),

$$\mathcal{O}_j \equiv \frac{1}{2}[N_d \mathrm{IOI} - (N_d - 1)\mathrm{IOI}^{(j)}] - \frac{N_p - 1}{2}, \quad (1)$$

where N_d is the number of constraints, N_p is the number of parameters, and $\mathrm{IOI}^{(j)}$ is the multidata set IOI for the (N_d–1) constraints, excluding the jth one. Given a set of constraints, the IOI quantifies their overall inconsistency and $\mathcal{O}_j$ tells us how incompatible each constraint is with the others. We show the results in Table 1. If one constraint has an $\mathcal{O}_j$ that is significantly higher compared to the others', that constraint is outlying. This is the case for CV SN, as shown in the first row of Table 1. The second row shows that removing CV SN from the constraint set reduces the IOI and most $\mathcal{O}_j$ (except for H0LiCOW), indicating that most other constraints are, overall, consistent with each other. Our numerical analysis also indicates that the second most outlying constraint is H0LiCOW. This can be seen (1) in the second row of Table 1, where H0LiCOW now has the highest $\mathcal{O}_j$ when CV SN is removed from the constraint list; and (2) in the third row, where the multidata set IOI further drops when H0LiCOW is removed in addition to CV SN, and all $\mathcal{O}_j$ are relatively small. It is important for the constraints to be obtained from different types of observations to avoid the possibility that some or most of them suffer from the same type of systematic effects. Planck and WMAP are both CMB observations and may have similar systematic effects. But after removing WMAP from the constraint set, CV SN still has the highest $\mathcal{O}_j$; as shown in the fourth row.

Both the constraint comparison shown in Figure 1 and this numerical analysis point to our conclusion that the local measurement is the strongest driver of the Hubble tension, followed by the time-delay strong-lensing result. Given the fact that most other constraints are overall consistent with each other, this favors the possibility that some previously unseen systematic effects exist in the two most outlying constraints. However, more independent observations are needed in the future for a more decisive conclusion.

Before we proceed, it is worth pointing out that Planck also has a relatively high $\mathcal{O}_j$, as seen from the first row in Table 1, despite the fact that the Planck constraint overlaps with the white circle well (although not perfectly). But Planck's relatively high $\mathcal{O}_j$ is mainly driven by CV SN and H0LiCOW, which can been seen from the fact that Planck's $\mathcal{O}_j$ drops significantly after CV SN alone or both CV SN and H0LiCOW are removed from the comparison; see the second and third rows in Table 1. As we will further discuss later, there is some tension within the two most precise local measurements of H_0 (Freedman et al. 2020), and a recent analysis of time-delay strong lensing gives a larger uncertainty and somehow lower value of H_0 (Birrer et al. 2020). Using either alternative to these two constraints indeed significantly lowers most of the $\mathcal{O}_j$; see the sixth and seventh rows in Table 1. On the other hand, since Planck is the strongest constraint, if it is particularly incompatible with most of the other constraints, removing it from the analysis should lead to an even more significant drop of $\mathcal{O}_j$. But this is not the case. As we can see from the fifth row of Table 1, a few $\mathcal{O}_j$ still remain relatively high after Planck is removed from the analysis. This reflects the fact, mentioned earlier, that CV SN tends to overlap with different constraints in different parameter regions.

However, we would like to make clear that the consistency between Planck and most other observations found here does not imply a resolution or denial of the "σ_8 tension." The Planck result has been shown to be in conflict with the inferred σ_8 (or some other combinations of σ_8 and Ω_m) from most LSS observations (Boruah et al. 2020; Joudaki et al. 2020; Wibking et al. 2020), though not all (Hamana et al. 2020). Investigating the σ_8 tension is beyond the scope of this work. Nonetheless, we find that the Planck constraint does not on its own drive the current H_0 tension.

3. Nonstandard Cosmology

Our analysis above examines the consistency of current constraints assuming a spatially flat ΛCDM model with no new physics. We emphasize that the above discussions are not rejecting the possibility of a nonstandard model that may reconcile all constraints considered. It is important to study nonstandard physics to see if the tension can be resolved. Our investigation is to serve as a complementary approach to the studies of nonstandard physics and provide a more comprehensive view of the current tension by including Ω_m rather than

looking at the tension in terms of H_0 alone. A plethora of models have been proposed in the literature. While a detailed discussion of each model is beyond our scope here, we provide a general discussion of how high-, mid-, and low-z nonstandard models, as well as local environmental factors, can alter constraints. It is important to note that any proposed model can change only a subset of constraints. This is another advantage of comparing constraints individually instead of combinations of subsets of them; it is easier to see which constraints can be changed in a proposed model. In Figure 1, we label each constraint with "H" (high-z), "M" (mid-z), "L" (low-z), or "E" (local/environmental) according to whether it can be changed by the corresponding models/proposals. (The H0LiCOW technique is relatively insensitive to the underlying cosmological model if the redshifts of the systems are not too high, so we leave it without a label.) Such a classification of the model dependences of each constraint is, to our knowledge, the first in the literature, which also helps navigate the search of nonstandard physics resolution. We discuss below whether these models/proposals can reconcile all the constraints in tension.

High-z models (H) here refer to those have some nonstandard physics before or around recombination but reduce to a ΛCDM universe thereafter (e.g., by $z \sim 100$). Examples are early-time dark energy[4] (Poulin et al. 2019), self-interacting neutrinos (Kreisch et al. 2020) and primordial magnetic fields Jedamzik & Pogosian (2020). Models of this category usually inject some extra energy before recombination, making the baryon–photon plasma sound horizon smaller. To compensate for this change and match the observed angular size of the sound horizon, the Hubble constant needs to be higher than the CMB-inferred value in the ΛCDM model. Also, there is a "theoretical correlation" between the late-time BAO and the CMB observations in the sense that they both involve the calculation of the BAO sound horizon (although at two different epochs).[5] It is therefore also possible for high-z models to reconcile the late-time BAO constraints with CV SN. However, since these models reduce to a ΛCDM universe after recombination, they cannot change the constraints from late-time observations, especially those from γ-ray, CC, cosmic age, and SN P. There would still be some tension remaining in the H_0–Ω_m space for CV SN and those late-time constraints. For example, the 2σ contour of the γ-ray constraint does not overlap with the region of ($H_0 \sim 74$ km s^{-1} Mpc^{-1}, Ω_m 0.3). In addition, if any star with an age $\gtrsim$13 Gyr is confirmed, it will disfavor high-z models as solutions to the tension.

Mid-z models (M) refer to those have some nonstandard physics after recombination but before $z \sim 6$. An example is fractional decaying dark matter with a lifetime $\lesssim$0.5 Gyr (Vattis et al. 2019). Mid-z models cannot change late-time constraints like γ-rays and CCs. They might be able to change and loosen the cosmic-age bounds, but this requires the cosmic expansion to be slower in the mid-redshift range (compared to a standard evolution of H) to compensate for the rising of today's H_0. If this decrease of the earlier cosmic expansion extended to the very early universe (before recombination), it would conflict with the CMB and late-time BAO observations, as slower cosmic expansion before recombination makes the sound horizon even larger.

Low-z models (L) refer to those have some nonstandard physics during a redshift range relevant for most of the late-time observations considered here (i.e., $z \lesssim 6$) but reduce to a standard cosmological model at higher redshifts. Recent examples are interacting dark energy (Pan et al. 2019), a rolling scalar field (Agrawal et al. 2019), and nonlocal modified gravity (Belgacem et al. 2018). Most of the constraints here would be affected in some way by late-time evolution; however, it has been argued that late-time models are not able to reconcile the Hubble constant tension (Evslin et al. 2018; Aylor et al. 2019). Observations such as BAO and SN Ia that probe the late-time background evolution can further constrain low-z models.

While the above models can alter many of the constraints, some proposals suggest that some local/environmental factors ($z \lesssim 0.03$; E) can bias the local determinations. Local factors do not pose a problem for the standard ΛCDM model at large scales but instead point to the need for a more detailed description of our local environment to account for such a systematic effect that can shift all local measurements in the same way. An example is a local underdense region (Shanks et al. 2019; Lombriser 2020). Recent studies have shown observational evidence supporting a small-scale local underdense region (Pustilnik et al. 2019; Böhringer et al. 2020). While it remains debated as to what extend this may alleviate the H_0 tension, it has been strongly argued that it is unlikely to play a substantial role and may bias the local measurement by at most 1% (Kenworthy et al. 2019).

What puts another challenge to environmental-factor explanations is the H0LiCOW result. This is because the H0LiCOW technique is not a local measurement,[6] although it is relatively insensitive to the underlying cosmological model. It involves observations at higher redshifts than those used for the local measurements, and a local structure, like a void, can barely shift the H0LiCOW result. Thus, separate considerations are needed to explain the high H0LiCOW result. Incidentally, some authors have suggested that the H0LiCOW technique can be affected by the mass-sheet degeneracy, and the issue may be more complicated than is assumed (Gomer & Williams 2019; Blum et al. 2020). Indeed, by relaxing the strong assumption on the lens density profile and adding more external data, Birrer et al. (2020) found that the uncertainty of H_0 is noticeably larger, with a lower mean value. As a consequence, using this TDSCOSMO result indeed of H0LiCOW in the numerical analysis makes CV SN more outlying and strengthens our conclusion; see the seventh row of Table 1.

Comparing different local measurements may provide hints for environmental effects, if any, but even some local measurements from different methods somewhat disagree. The recent TRGB-based local measurement reported $H_0 = 69.8 \pm 1.9$ km s^{-1} Mpc^{-1} (Freedman et al. 2019), which is more consistent with Planck than with CV SN. Other authors revisited this result and found a higher value, $H_0 = 72.4 \pm 2.0$ km s^{-1} Mpc^{-1} (Yuan et al. 2019). But Freedman et al. (2020) later showed more details of their analysis and confirmed their relatively low local measurement with $H_0 = 69.6 \pm 1.9$ km s^{-1} Mpc^{-1}. Using other methods to calibrate SNe Ia overall has relatively large uncertainties. Calibration using surface brightness fluctuations

[4] Debates are ongoing about whether LSS disfavors early dark energy models (Hill et al. 2020; Smith et al. 2020).

[5] This does not mean that the CMB and BAO are observationally dependent. We did not use any prior information from the CMB in the BAO constraints, but rather used BBN to constrain $\Omega_b h^2$.

[6] By local measurements, we refer to methods that are only based on the Hubble–Lemaître law and small-z ($z \lesssim 0.1$) observations.

(SBFs) gives $H_0 = 70.50 \pm 2.37(\mathrm{stat}) \pm 3.38(\mathrm{sys})\ \mathrm{km\,s^{-1}\,Mpc^{-1}}$ (Khetan et al. 2020), more consistent with the TRGB-based measurement. The Mira-based method reported $H_0 = 73.3 \pm 3.9\ \mathrm{km\,s^{-1}\,Mpc^{-1}}$ (Huang et al. 2020), more consistent with the CV SN result. These above local measurements are based on SNe Ia (using different calibrations); it is possible that they could share some common systematic effects. For example, the local H_0 may be overestimated if the Hubble-flow SNe Ia are intrinsically brighter than those in the calibration samples due to a difference in environmental age (Rigault et al. 2018; Kang et al. 2020; but see also Rose et al. 2019 for discussion). Or, there might be other nonstandard physical reasons, such as screened fifth forces that affect the calibration of SNe Ia (Desmond et al. 2019).

Replacing SNe Ia with other secondary distance indicators can test the possible unaccounted-for systematic errors on the SN Ia side. For example, it was recently reported that $H_0 = 76.0 \pm 2.5\ \mathrm{km\,s^{-1}\,Mpc^{-1}}$ using the Tully–Fisher relation (TFR; Kourkchi et al. 2020). A similar result was obtained using the baryonic TFR (Schombert et al. 2020). With a larger uncertainty, de Jaeger et al. (2020) reported $H_0 = 75.8^{+5.2}_{-4.9}\ \mathrm{km\,s^{-1}\,Mpc^{-1}}$ using SNe II. These works, however, used Cepheid variables or TRGBs in calibration and thus are not totally independent local measurements. As such, differences in the TRGB calibrations lead to complicated agreements or discrepancies among different local measurements (Kourkchi et al. 2020). There are local determinations that do not require the distance ladder or SNe Ia, such as the MCP result (Pesce et al. 2020) and the standard siren multimessenger method (LIGO Scientific Collaboration, the Virgo Collaboration et al. 2019). The latest MCP result is $73.9 \pm 3.0\ \mathrm{km\,s^{-1}\,Mpc^{-1}}$. This is a relatively weak constraint and consistent with most of the other constraints considered here. The gravitational-wave multimessenger constraint is still too weak to play a significant role.

4. Discussion

We present these results as an exploration of the range of possibilities for approaching tensions among these disparate data sets. It should be noted that our numerical analysis does not include the cosmic-age bounds, since single-sided constraints cannot be considered in the moment-based IOI formalism. However, considering these bounds can only strengthen our conclusion, since they overall put pressure on the regions where CV SN overlaps with SNe Ia and DES, as well as the region where it overlaps with BAO Gal. As mentioned earlier, the recent TRGB-based determination of H_0 is lower than that of CV SN (Freedman et al. 2020). If we replace CV SN with this result and redo our numerical analysis, IOI and most $\mathcal{O}_j$ (except for H0LiCOW) are significantly reduced; see the sixth row in Table 1. We can also see the consistency between the TRGB result and most other constraints; see Appendix D. In addition to replacing CV SN with TRGB, removing H0LiCOW further enhances the consistency among constraints; see the seventh row in Table 1. Recently, Ivanov et al. (2020) and Philcox et al. (2020) improved the analysis of the galaxy power spectrum (embedding BAO) at $z_{\mathrm{eff}} = 0.38$ and 0.61 using different methods that account for nonlinear clustering and a range of other effects. Their constraints on the H_0–Ω_{m} plane also fall into the guiding circle in Figure 1.

A caveat in our investigation is that all observations are treated upon the same footing in the sense that no single one of them is considered more reliable than any other. In practice, some results may be more or less vulnerable to systematic effects. In particular, while promising, the CC constraint is a relatively new technique, and studies of additional systematic errors are ongoing (Moresco et al. 2020). We note, however, that our CC constraint has included the estimated additional systematic errors considered in Moresco et al. (2020); see our Appendix B. As mentioned earlier, a better understanding and constraining of the lens model is required before a robust constraint on H_0 from strong gravitational lensing can be achieved (Birrer et al. 2020). In addition, knowing the cosmic age is promising to constitute a strong test to high-z (and likely also mid-z) models. In fact, any objects or methods that confirm a cosmic age $\gtrsim$13.5 Gyr since $z = 100$ (e.g., if the aforementioned estimated age of J18082002–5104378 A, 13.535 ± 0.002 Gyr, is confirmed) can rule out all high-z solutions to the current H_0 tension.

5. Conclusions

We have shown that it is very beneficial to compare constraints as individually as possible in the H_0–Ω_{m} space when investigating the H_0 tension. It allows us to more robustly see how different constraints behave in the standard ΛCDM model, as well as to more easily tell whether a nonstandard model can reconcile all constraints.

We have performed a systematic comparison of various constraints from different observations in the H_0–Ω_{m} space based on the standard ΛCDM model. Most constraints consistently overlap along different degeneracy directions in some common region in the H_0–Ω_{m} plane centered around the general vicinity of (68.5, 0.3). The fact that the Cepheid-based local determination of H_0 does not overlap with such a common region suggests that the main driver of the tension may be supposed to be the local measurement(s). The time-delay strong-lensing result only marginally overlaps with that region, making it the next most outlying constraint. While we do not reject the possibility that some nonstandard physics may resolve the current Hubble constant tension, we found that it is difficult for high-, mid-, or low-z nonstandard evolution models or local environmental factors to reconcile the constraints of all of the considered observations as they stand. Confirming the results from γ-ray attenuation and CCs, as well as the lower limit of cosmic age, can rule out high- and mid-z models that try to resolve the current H_0 tension. Standard rulers and candles will continue to put pressure on low-z models. Solutions that alter the local determination need a separate explanation for the high time-delay strong-lensing result.

In the future, there will be more and more independent methods to constrain the cosmic evolution. For instance, observing the redshift drift will allow us to directly detect the real-time cosmic expansion (Loeb 1998). The BAO constraints will be improved from the line-intensity mapping of emission from star-forming galaxies (Bernal et al. 2019) and the next-generation galaxy surveys (Bengaly et al. 2020). The drop-off in the abundance of $\gtrsim 45\ M_\odot$ black holes can be used to probe cosmic expansion by making binary black hole mergers "standardizable" (Farr et al. 2019). Velocity-induced acoustic oscillations, a standard ruler that can be seen in the 21 cm power spectrum, provide a way to probe the background evolution at cosmic dawn (Muñoz 2019). And standard siren multimessengers provide another way to measure H_0. Comparing them all in the H_0–Ω_{m} space can help us to more easily discover the fundamental cause of the Hubble constant tension.

It is exciting to see whether the current Hubble constant tension is leading us to another new understanding of the universe. We hope that this analysis motivates a new way of considering the various cosmological constraints and a different perspective on viewing such a tension.

We thank Alberto Domínguez Díaz and Radoslaw Jan Wojtak for providing the MCMC chain of the analysis to the γ-ray attenuation data; Simon Birrer, Mustapha Ishak, Khaled Said, Brian Schmidt, Ji Yao, and Matias Zaldarriaga for useful comments and suggestions; Adam Mantz and Sebastian Bocquet for answering questions on some particular cosmological constraints; and Adam Riess for helpful discussions and references. We especially thank Michele Moresco for the advice on how to consider additional systematic errors in the current CC data. K.J.M. acknowledges the Simons Emmy Noether Fellowship, which supported her residence at the Perimeter Institute while the later stages of this work were carried out. We also thank an anonymous referee for feedback and suggestions that have improved this work.

Appendix A
Likelihood of Lens System DES J0408

The latest joint H0LiCOW analysis only includes six lens systems (Wong et al. 2020), while there has been an individual analysis of a seventh lens system, DES J0408 (Shajib et al. 2020). The analysis of DES J0408 alone gives $H_0 = 74.0^{+2.7}_{-3.0}$ km s^{-1} Mpc^{-1} in the standard ΛCDM model. While the chains of the time-delay distance $D_{\Delta t}$ and the lens angular diameter distance $D_{\rm L}$ for this system are not publicly available, we approximated the likelihoods of $D_{\Delta t}$ and $D_{\rm L}$ for lens DES J0408 by a skewed Gaussian distribution,

$$\mathcal{L}(x) \propto \left[1 + \mathrm{erf}\left(s\frac{x - x_0}{\sigma}\right)\right]\exp\left(-\frac{(x - x_0)^2}{2\sigma^2(1 + |s|)}\right), \quad \text{(A1)}$$

where x stands for $D_{\Delta t}$ or $D_{\rm L}$ in megaparsecs. The parameters (x_0, σ, s) are different for $D_{\Delta t}$ and $D_{\rm L}$. They are chosen to reproduce the median statistics of $D_{\Delta t} = 3382^{+146}_{-115}$ and $D_{\rm L} = 1711^{+376}_{-280}$ Mpc reported in Shajib et al. (2020) and are (3231, 133.5, 1.17) for $D_{\Delta t}$ and (1368, 331.4, 1.37) for $D_{\rm L}$. We have ignored the correlation between $D_{\Delta t}$ and $D_{\rm L}$. Using the same priors on H_0 and $\Omega_{\rm m}$ in Shajib et al. (2020), we closely reproduced the posterior $H_0 = 74.0^{+2.7}_{-3.1}$ km s^{-1} Mpc^{-1} for lens DES J0408–5354 after marginalizing over $\Omega_{\rm m}$. The two likelihoods of $D_{\Delta t}$ or $D_{\rm L}$ are then added to the joint H0LiCOW likelihood. The joint marginalized constraint on H_0 is $73.7^{+1.5}_{-1.6}$ km s^{-1} Mpc^{-1} for all seven lens systems.

Appendix B
Estimating Systematic Errors for CC Data

Systematic effects for the CC measurements have been extensively considered in Moresco et al. (2020). While their previous works considered systematic errors due to the young component contamination and the star formation history dependence (Moresco et al. 2016; Moresco & Marulli 2017), Moresco et al. (2020) focused on additional systematic errors due to the initial mass function (IMF) and stellar population synthesis (SPS) model. We added these to the covariance matrices of the current CC data to better represent the full range of errors. Specifically, we utilized columns (2) and (5) in Moresco et al.'s (2020) Table 3 for these two systematic errors. When using column (5), we assumed that the most discordant SPS model(s) can be discarded. This is fairly reasonable because for the SPS models available in the literature, Moresco et al. (2020) found that one of them is significantly different from the others, while the others are in fair agreement. Therefore, we compared against high signal-to-noise ratio and high spectral data to see which SPS model(s) is (are) better, which can be achieved by using the new high-resolution instruments, e.g., X-Shooter or VIMOS/HR-Red. We interpolated the data listed in their Table 3 to get the error budget of the current CC data at each redshift due to these two extra sources. We then built the covariance matrices, $\mathrm{Cov}^{\rm IMF}_{\rm i,j}$ and $\mathrm{Cov}^{\rm SPS}_{\rm i,j}$, according to their Equation (9), i.e.,

$$\mathrm{Cov}^{\rm X}_{i,j} = \widehat{\eta^{\rm X}}(z_i)H(z_i)\,\widehat{\eta^{\rm X}}(z_j)H(z_j), \quad \text{(B2)}$$

where $\widehat{\eta^{\rm X}}(z)$ are obtained by interpolation with the data provided in their Table 3, and $H(z_i)$ are CC measurements at different redshifts. At last, we added $\mathrm{Cov}^{\rm IMF}_{\rm i,j}$ and $\mathrm{Cov}^{\rm SPS}_{i,j}$ to the covariance matrix of the current CC data and performed a likelihood analysis with the standard ΛCDM model to obtain the CC constraint in the H_0–$\Omega_{\rm m}$ plane. We note that the estimated $\mathrm{Cov}^{\rm IMF}_{\rm i,j}$ and $\mathrm{Cov}^{\rm SPS}_{\rm i,j}$ according to Equation (B2) are correlated at all redshifts. But, as pointed out in Moresco et al. (2020), no model systematically overpredicts or underpredicts the Hubble parameter with respect to another, so these systematic errors are not quite correlated at different redshift bins. However, we choose to include the correlation of those extra systematic errors; therefore, the constraint given here should be viewed as a conservative estimate. Detailed consideration of additional systematic errors for CC constraints is a work in progress (Moresco et al. 2020).

Appendix C
Remarks on the Combination of BAO and BBN

In the context of the standard ΛCDM model,[7] combining BAO with the baryon density parameter inferred from BBN has become a standard procedure to provide a statistically independent constraint on H_0 (Cuceu et al. 2019; Schöneberg et al. 2019). However, when the baryon acoustic sound horizon scale at the drag epoch $r_{\rm d}$ is treated as a free parameter, BAO alone is not able to constrain H_0 (Aylor et al. 2019). This is because $r_{\rm d}$ is degenerate with H_0 and needs to be known to constrain H_0 from BAO. This $r_{\rm d}$ can be modeled once a cosmological model is assumed, such as the standard ΛCDM model in our main analysis. The calculation of $r_{\rm d}$ only involves physics before the drag epoch ($z_{\rm d} \sim 1060$; Planck Collaboration et al. 2018); as such, $r_{\rm d}$ is often said to be "calibrated at early time." One may argue that r_d can also be calibrated (or, more properly, inferred) if we treat it as a free parameter and combine BAO with some local measurement of H_0 (Addison et al. 2018), since knowing H_0 gives us $r_{\rm d}$ from BAO. However, inferring $r_{\rm d}$ in this way already assumes the local measurement used to infer the sound horizon scale to be correct and that there is some beyond-the-standard-ΛCDM physics. This approach does not match our goal. This is because the first

[7] By the standard ΛCDM model, we refer to one with the number of effective relativistic particles, neutrino mass, spatial curvature, etc., fixed to the standard values (Planck Collaboration et al. 2018).

part of this work investigates which method(s) give the most incompatible constraint(s) in the H_0–Ω_m plane to the others when the standard ΛCDM model is assumed. It would be an unfair comparison to relax the assumption of the standard ΛCDM model for BAO while keeping this assumption for other constraints. However, we provide a general discussion of nonstandard models in Section 3.

The BBN provides a prior on the reduced baryon fraction $\Omega_b h^2$, about which there is no substantial disagreement from different observations based on completely different physics, e.g., CMB anisotropies (Planck Collaboration et al. 2018). The $\Omega_b h^2$ values inferred from various different effects on CMB anisotropies are also consistent with each other (Motloch 2020). This gives us some confidence in the robustness of this prior on $\Omega_b h^2$. It was also pointed out in Verde et al. (2019) that, for a nonstandard model proposed to resolve the H_0 tension, "any change in background parameters (physical densities) should be mostly via H_0 and not via the density parameters themselves." Furthermore, Cuceu et al. (2019) and Schöneberg et al. (2019) showed that the current BAO results only have a weak dependence on $\Omega_b h^2$, and we have adopted an even weaker BBN prior on $\Omega_b h^2 = 0.0222 \pm 0.0005$ than those adopted in Cuceu et al. (2019) and Schöneberg et al. (2019).

One may worry that the same BBN constraint is included in both BAOs, which may render the two BAO results not independent. To dispel this latter worry, we perform a numerical analysis with both BAOs combined so that BBN is used only once. Doing so does not qualitatively change our conclusions; see the last row in Table 1.

Appendix D
Other Local Measurements and LSS Constraints

Here we include versions of Figure 1, plotting other local measurements (TRGB and MCP) in place of the CV SN constraint. We also plot SPT SZ in both panels. In our numerical analysis in the previous sections, CV SN is replaced by TRGB in some cases to see how this alternative distance ladder measurement compares to other constraints, but MCP, as an independent local measurement, is always included. In the left panel of Figure 2, we plot the TRGB constraint, and in the right panel, we plot all of the quoted local measurements. The thick and thin bars in the right panel represent 1σ and 2σ confidence ranges, respectively, and should be interpreted as vertical bands. We note that not all local measurements are independent, so in our numerical analyses, we did not include all of them at the same time but alternatively used the CV SN and TRGB results; see Section 3 for a discussion. As can be seen in the right panel, the independent MCP constraint prefers a high H_0 value but is broader than the CV SN allowed region and therefore has some overlap with the guiding white circle (with the 2σ contour). The TRGB constraint is in better agreement with other constraints, substantially overlapping the white guiding circle. Quantitatively, the level of concordance can be seen in Table 1 and discussions thereof. It is worth mentioning that the joint analysis of 6dFGS and Sloan Digital Sky Survey peculiar velocity results indicates some indirect preference for $H_0 > 70$ km s^{-1} Mpc^{-1} and (when combined with other probes as needed) may also provide an interesting constraint on the H_0–Ω_m plane (Said et al. 2020).

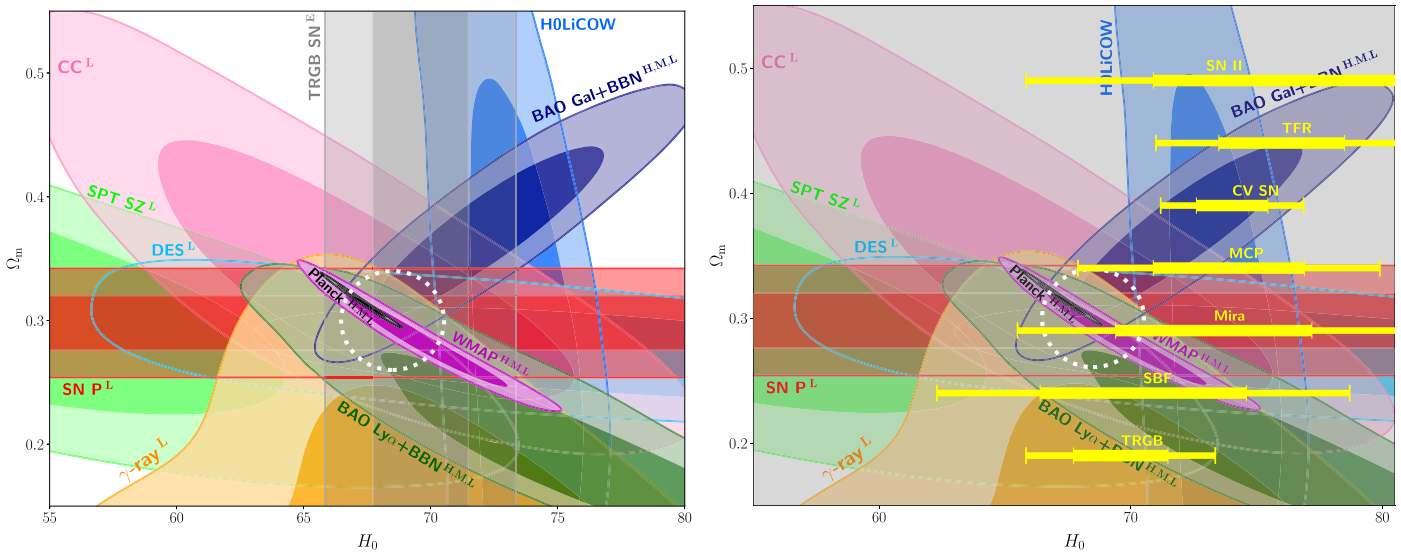

Figure 2. Different constraints in the H_0 and Ω_m space based on a flat ΛCDM model, as in Figure 1. As above, dark and light contours show the 68% and 95% confidence regions of each posterior. Here the cosmic-age bound is omitted. In the left panel, we plot the TRGB constraint instead of CV SN, and on the right, we plot all of the quoted local measurements of H_0 in Section 3. The error bars in the right panel should be interpreted as vertical bands, with the thick and thin lines representing 1σ and 2σ confidence ranges, respectively. Local measurements tend to give a higher H_0 value than indicated by the white circle. However, we note that they are not all independent from each other, and their favored ranges depend on the calibration adopted; see the end of Section 3 for a discussion. In both panels, we included the constraints from SPT SZ clustering (lime), for which we restrict that $0.0006 \leqslant \Omega_\nu h^2 \leqslant 0.0009$ for the standard ΛCDM, since the chains obtained from https://pole.uchicago.edu are based on a $\nu\Lambda$ CDM model with a large range of $\Omega_\nu h^2$.

ORCID iDs

Weikang Lin https://orcid.org/0000-0003-2240-7031
Katherine J. Mack https://orcid.org/0000-0001-8927-1795

References

Abbott, T. M. C., Abdalla, F. B., Alarcon, A., et al. 2018, PhRvD, 98, 043526
Addison, G. E., Watts, D. J., Bennett, C. L., et al. 2018, ApJ, 853, 119
Agrawal, P., Obied, G., & Vafa, C. 2019, arXiv:1906.08261
Alam, S., Ata, M., Bailey, S., et al. 2017, MNRAS, 470, 2617
Ata, M., Baumgarten, F., Bautista, J., et al. 2018, MNRAS, 473, 4773
Aylor, K., Joy, M., Knox, L., et al. 2019, ApJ, 874, 4
Belgacem, E., Dirian, Y., Foffa, S., & Maggiore, M. 2018, JCAP, 03, 002
Bengaly, C. A. P., Clarkson, C., & Maartens, R. 2020, JCAP, 05, 053
Bernal, J. L., Breysse, P. C., & Kovetz, E. D. 2019, PhRvL, 123, 251301
Beutler, F., Blake, C., Colless, M., et al. 2011, MNRAS, 416, 3017
Birrer, S., Shajib, A. J., Galan, A., et al. 2020, A&A, 643, A165
Blomqvist, M., du Mas des Bourboux, H., Busca, N. G., et al. 2019, A&A, 629, A86
Blum, K., Castorina, E., & Simonović, M. 2020, ApJL, 892, L27
Bocquet, S., Dietrich, J. P., Schrabback, T., et al. 2019, ApJ, 878, 55
Böhringer, H., Chon, G., & Collins, C. A. 2020, A&A, 633, A19
Boruah, S. S., Hudson, M. J., & Lavaux, G. 2020, MNRAS, 498, 2703
Cooke, R. J., Pettini, M., & Steidel, C. C. 2018, ApJ, 855, 102
Cuceu, A., Farr, J., Lemos, P., & Font-Ribera, A. 2019, JCAP, 10, 044
de Jaeger, T., Stahl, B. E., Zheng, W., et al. 2020, MNRAS, 496, 3402
Desmond, H., Jain, B., & Sakstein, J. 2019, PhRvD, 100, 043537
Dhawan, S., Brout, D., Scolnic, D., et al. 2020, ApJ, 894, 54
Domínguez, A., Wojtak, R., Finke, J., et al. 2019, ApJ, 885, 137
Evslin, J., Sen, A. A., & Ruchika 2018, PhRvD, 97, 103511
Farr, W. M., Fishbach, M., Ye, J., & Holz, D. E. 2019, ApJL, 883, L42
Freedman, W. L., Madore, B. F., Hatt, D., et al. 2019, ApJ, 882, 34
Freedman, W. L., Madore, B. F., Hoyt, T., et al. 2020, ApJ, 891, 57
Gomer, M. R., & Williams, L. L. R. 2019, arXiv:1907.08638
Hamana, T., Shirasaki, M., Miyazaki, S., et al. 2020, PASJ, 72, 16
Hill, J. C., McDonough, E., Toomey, M. W., & Alexander, S. 2020, PhRvD, 102, 043507
Hinshaw, G., Larson, D., Komatsu, E., et al. 2013, ApJS, 208, 19
Huang, C. D., Riess, A. G., Yuan, W., et al. 2020, ApJ, 889, 5
Ivanov, M. M., Simonović, M., & Zaldarriaga, M. 2020, JCAP, 05, 042
Jedamzik, K., & Pogosian, L. 2020, PhRvL, 125, 181302
Jimenez, R., Cimatti, A., Verde, L., Moresco, M., & Wandelt, B. 2019, JCAP, 03, 043
Joudaki, S., Hildebrandt, H., Traykova, D., et al. 2020, A&A, 638, L1
Kang, Y., Lee, Y.-W., Kim, Y.-L., Chung, C., & Ree, C. H. 2020, ApJ, 889, 8
Kenworthy, W. D., Scolnic, D., & Riess, A. 2019, ApJ, 875, 145
Khetan, N., Izzo, L., Branchesi, M., et al. 2020, arXiv:2008.07754
Kourkchi, E., Tully, R. B., Anand, G. S., et al. 2020, ApJ, 896, 3
Kreisch, C. D., Cyr-Racine, F.-Y., & Doré, O. 2020, PhRvD, 101, 123505
Lewis, A., & Bridle, S. 2002, PhRvD, 66, 103511
Lin, W., & Ishak, M. 2017, PhRvD, 96, 023532
Lin, W., & Ishak, M. 2019, arXiv:1909.10991
Loeb, A. 1998, ApJ, 499, L111
Lombriser, L. 2020, PhLB, 803, 135303
Mantz, A. B., Allen, S. W., Morris, R. G., et al. 2014, MNRAS, 440, 2077
Moresco, M., Jimenez, R., Verde, L., Cimatti, A., & Pozzetti, L. 2020, ApJ, 898, 82
Moresco, M., & Marulli, F. 2017, MNRAS, 471, L82
Moresco, M., Pozzetti, L., Cimatti, A., et al. 2016, JCAP, 05, 014
Motloch, P. 2020, PhRvD, 101, 123509
Muñoz, J. B. 2019, PhRvL, 123, 131301
O'Malley, E. M., Gilligan, C., & Chaboyer, B. 2017, ApJ, 838, 162
Pan, S., Yang, W., Di Valentino, E., Saridakis, E. N., & Chakraborty, S. 2019, PhRvD, 100, 103520
Pesce, D. W., Braatz, J. A., Reid, M. J., et al. 2020, ApJL, 891, L1
Philcox, O. H. E., Ivanov, M. M., Simonović, M., & Zaldarriaga, M. 2020, JCAP, 05, 032
Planck Collaboration, Aghanim, N., Akrami, Y., et al. 2018, A&A, 641, A6
Poulin, V., Smith, T. L., Karwal, T., & Kamionkowski, M. 2019, PhRvL, 122, 221301
Pustilnik, S. A., Tepliakova, A. L., & Makarov, D. I. 2019, MNRAS, 482, 4329
Riess, A. G., Casertano, S., Yuan, W., Macri, L. M., & Scolnic, D. 2019, ApJ, 876, 85
Rigault, M., Brinnel, V., Aldering, G., et al. 2018, arXiv:1806.03849
Rose, B. M., Garnavich, P. M., & Berg, M. A. 2019, ApJ, 874, 32
Ross, A. J., Samushia, L., Howlett, C., et al. 2015, MNRAS, 449, 835
Said, K., Colless, M., Magoulas, C., Lucey, J. R., & Hudson, M. J. 2020, MNRAS, 497, 1275
Sandage, A. R. 1970, PhT, 23, 34
Schlaufman, K. C., Thompson, I. B., & Casey, A. R. 2018, ApJ, 867, 98
Schombert, J., McGaugh, S., & Lelli, F. 2020, AJ, 160, 71
Schöneberg, N., Lesgourgues, J., & Hooper, D. C. 2019, JCAP, 10, 029
Scolnic, D. M., Jones, D. O., Rest, A., et al. 2018, ApJ, 859, 101
Shajib, A. J., Birrer, S., Treu, T., et al. 2020, MNRAS, 494, 6072
Shanks, T., Hogarth, L. M., & Metcalfe, N. 2019, MNRAS, 484, L64
Smith, T. L., Poulin, V., Bernal, J. L., et al. 2020, arXiv:2009.10740
The LIGO Scientific Collaboration, the Virgo Collaboration, Abbott, B. P., et al. 2019, arXiv:1908.06060
VandenBerg, D. A., Bond, H. E., Nelan, E. P., et al. 2014, ApJ, 792, 110
Vattis, K., Koushiappas, S. M., & Loeb, A. 2019, PhRvD, 99, 121302
Verde, L., Treu, T., & Riess, A. G. 2019, NatAs, 3, 891
Wibking, B. D., Weinberg, D. H., Salcedo, A. N., et al. 2020, MNRAS, 492, 2872
Wong, K. C., Suyu, S. H., Chen, G. C.-F., et al. 2020, MNRAS, 498, 1420
Yuan, W., Riess, A. G., Macri, L. M., Casertano, S., & Scolnic, D. 2019, ApJ, 886, 61